PCCP

ROYAL SOCIETY OF CHEMISTRY

PAPER

View Article Online
View Journal | View Issue

Cite this: *Phys. Chem. Chem. Phys.*, 2024, **26**, 12600

Theoretical structural and spectroscopic characterization of peroxyacetic acid (CH_3–CO–OOH): study of the far infrared region†

Sinda Brahem,[abc] Dorsaf Missaoui,[abc] Ounaies Yazidi,[a] Faouzi Najar [a] and María Luisa Senent *[bc]

Peroxyacetic acid, a non-rigid oxygenated organic molecule which acts in the atmosphere as a reservoir of HO_X and RO_X radicals, is studied using highly correlated *ab initio* methods with the aim of its spectroscopic characterization in the gas phase. The study focuses on the far infrared region providing reliable rovibrational parameters such as energy levels and splittings. The molecule presents three conformers that inter-convert by internal rotation, drawing a potential energy surface of 12 minima. One of them shows prominent stability due to the formation of one weak intramolecular bond between the hydrogen atom of the hydroperoxy group and the oxygen atom of the carbonyl group. For the three minimum energy structures, rotational constants and centrifugal distortion constants are provided. It may be expected that the most stable conformer is the only one contributing to the spectral features in further measurements at low temperature. In this structure, the methyl torsional barrier has been found to be very low, V_3 = 88.6 cm^{-1} producing a splitting of 2.262 cm^{-1} for the ground vibrational state. The study confirms that the ν_{20} torsional mode interacts strongly with the other two torsional modes ν_{19} and ν_{21}, but slightly with the remaining vibrations. Then, a variational procedure in three dimensions allows the exploration of the low-frequency modes. The methyl torsional fundamental ν_{21} was found to be 49.1 cm^{-1} (A_i) and 33.4 cm^{-1} (E). The fundamentals of ν_{20} (C–O bond torsion) and ν_{19} (OH torsion) have been computed to be 216.7 cm^{-1} (A_2) and 218.5 cm^{-1} (E) and 393.6 cm^{-1} (A_2) and 394.1 cm^{-1}. Since non-rigidity can have effects on the reactivity due to the conformer interconversion, and transitions involving low-lying levels can be observed with many spectroscopic techniques, this work can help kinetic studies and assignments of further spectroscopic studies needed for the detection in the gas phase of trace molecules.

Received 27th November 2023,
Accepted 20th March 2024

DOI: 10.1039/d3cp05783f

rsc.li/pccp

1. Introduction

Organic peroxides represent oxygenated organic molecules (OOMs) that can act as reservoirs of the HO_X and RO_X radicals in the atmosphere.[1,2] They are receiving much research attention due to their potential role in enhancing tropospheric oxidation capacity[1–3] as well as early phases of secondary aerosol formation.[4] Organic peroxides generally form in the atmosphere *via* OH mediated oxidation of saturated and unsaturated hydrocarbons.[5,6] They have a significant impact on air quality and human health.[7] The toxic effects of oxygen species in atmospheric aerosols on human health have been emphasized,[8] motivating their detection in urban areas.[9–11]

Gas-phase OOMs can contribute substantially to the growth of newly formed particles.[9] Recent reviews attend to the relevance of OOM peroxides in the chemistry of the atmosphere.[12,13] OOMs are emitted into the atmosphere from natural and anthropogenic sources, and they are formed in the atmosphere as oxidation products of all hydrocarbons present in the atmosphere.[12] Low-volatility multifunctional oxygenated organic compounds condense onto existing atmospheric particles and hence increase the organic fraction content of secondary organic aerosols.[12] Noziere *et al.*[13] reviewed the different techniques available today to characterize atmospheric organic compounds. They analyzed the efficiency of rovibrational spectroscopy for the trace molecule identification.

The subgroup of peroxycarboxylic acids (RCO–OOH) is considered as important intermediates in the oxidation of volatile organic compounds.[14] The simple and abundant one, peroxyacetic acid (peracetic acid, PAA, CH_3CO–OOH), is a colorless

[a] *Laboratoire de Spectroscopie Atomique Moléculaire et Applications, Faculté des Sciences de Tunis, Université de Tunis El Manar, 2092, Tunisia*
[b] *Departamento de Química y Física Teóricas, Instituto de Estructura de la Materia, IEM-CSIC, Serrano 121, Madrid 28006, Spain*
[c] *Unidad Asociada GIFMAN, CSIC-UHU, Spain. E-mail: ml.senent@csic.es*

† Electronic supplementary information (ESI) available. See DOI: https://doi.org/10.1039/d3cp05783f

liquid with melting and boiling points of 0.1 °C and 105 °C, respectively. It has been widely detected in the terrestrial atmosphere.[15] It has been shown that the local photochemical production was the major source of PAA, and its concentration increased with increasing temperature, solar radiation and ozone but decreased with increasing NO_x (NO and NO_2), CO, SO_2, and relative humidity.[15] PAA is considered to be the third most common urban peroxide after hydrogen peroxide and methyl hydroperoxide. It contributes to the oxidation of SO_2 and HSO_3 in the atmosphere.[16] Its dissociation has been studied by UV laser photolysis in the gas phase producing $CH_3 + CO_2 + OH$.[17]

PAA concentrations have been detected in plumes from biomass burning.[18] PAA can be formed in the atmosphere through the reactions of H_2O or HO_2 with free radicals such as $CH_3CO–OO$, or through the reaction of O_3 with acetic acid.[19] The photolysis of biacetyl in aqueous aerosols, fogs, and clouds produces PAA.[20] PAA competes with the formation of peroxyacyl nitrate (PAN = $CH_3CO–OONO_2$), a peroxyacetic acid-nitronium ion complex playing a vital role in the global distribution of tropospheric ozone.[21]

The aim of this work is to perform spectroscopic characterization of PAA for which extremely limited spectroscopic experimental and theoretical information are available. The first spectroscopic studies occurred in the fifties. In 1952, Giguère *et al.*[22] published the infrared spectrum of performic and peracetic acids focusing on the effect of the intramolecular hydrogen bond on the band positions and stabilities and comparing the spectra with those of formic acid and acetic acid. They provide band center positions in the vapor phase in the region between 3570 cm^{-1} and 648 cm^{-1}. Based on their observations, they concluded that a stable five-membered ring conformer, resulting from the formation of an intramolecular hydrogen bond between the carbonyl oxygen and the hydrogen of the hydroxyl group, represents the predominant structure.

Later, Cugley *et al.*[23] recorded the infrared spectrum in Ar and N_2 matrices of PAA and three deuterated varieties, $CH_3CO–OOD$, $CD_3CO–OOD$ and $CD_3CO–OOD$, at 4 K. The observed vibrational bands were assigned to the most stable PAA geometry stabilized by the intramolecular H-bond, previously reported by Giguere *et al.*[22] They provide force constants and thermodynamic functions. In another publication, Cugley *et al.*[24] analyzed the microwave spectrum of $CH_3CO–OOH$ and $CH_3CO–OOD$ in the gas phase, in the range from 12 to 40 GHz. They estimated the methyl torsional barrier to be very low (V_3 = 76.70 (45) cm^{-1}). From the Stark effect, the dipole moment components were determined to be μ_a = 2.294(3) D, μ_b = 0.650(4) D and μ = 2.384(5) D.[23] The three rotational constants were estimated to be A_0 = 10 814.95 MHz, B_0 = 4275.06 MHz and C_0 = 3122.64 MHz.[23]

The effect of the weak intramolecular hydrogen bond on the OH stretching transitions in peroxyformic acid and peroxyacetic acid was studied by Hazra et Sinha.[25,26] The vapor phase absorption spectra and the integrated band intensities of the OH stretching fundamental, as well as first and second overtones ($2\nu_{OH}$ and $3\nu_{OH}$) of peroxyacetic acid (PAA) were measured using a combination of FT-IR and photoacoustic spectroscopy.[26] The authors compared theoretical calculations at the MP2 and CCSD levels of theory with the observations and found strong disagreements between the measured and calculated integrated absorption cross sections of the $1\nu_{OH}$, $2\nu_{OH}$ and $3\nu_{OH}$.[26]

Peroxyacetic acid has been the object of various theoretical works.[27–29] The proton affinity has been computed using *ab initio* methods by Miller and Francisco.[30] These authors, with the goal of better understanding the proton affinity of PAN,[31] provide a systematic investigation of the structure, harmonic force field, and proton affinity[31] using Density Functional Theory and MP2 and QCISD *ab initio* methods.

The present paper aims at the spectroscopic characterization of PAA with a special mention to the Far Infrared region. We search for very accurate molecular properties that can help the interpretation of further investigations. The calculations of the equilibrium structures and potential energy surface are performed using highly correlated *ab initio* methods and procedures previously tested in studies of alike molecules.[32–35] Given the lack of previous research, most of our findings are predictions that cannot be compared with the existing experimental data. In these cases, the goal is to obtain new spectroscopic data that might help the interpretation of far-infrared measurements and the assignment of rotational and rovibrational spectra. For the far infrared region, we employed a variational procedure in three dimensions whose independent variables are the internal rotations responsible for the interconversion of the minima. This allows very low energy levels to be obtained and their torsional subcomponents that can be involved in transitions observable using different spectroscopic techniques in different spectral regions.

Identification of trace molecules in the atmosphere through rovibrational spectroscopy requires a previous laboratory characterization. In the case of non-rigid species, assignments of the measurements are complex. A previous theoretical study describing the FIR region can help further experimental work. The conformational analysis can help kinetic studies.

2. Results and discussion

2.1. Electronic structure calculations

The structural parameters related to the minimum-energy structures of PAA were computed using explicitly correlated coupled cluster theory with single and double substitutions augmented by a perturbative treatment of triple excitations (CCSD(T)-F12b)[36,37] as it is implemented in Molpro[38] version 2022 and selecting the default options. A correlation consistent basis set, cc-pCVTZ-F12 (denoted by CVTZ-F12 in this paper), optimized for accurately describing core–core and core-valence correlation effects with explicitly correlated F12 method, was employed.[39]

Two different pathways were used to obtain spectroscopic parameters: (a) vibrational second-order perturbation theory (VPT2)[40] implemented in the Gaussian version C.01[41] which

starting point are anharmonic force fields computed using second-order Möller–Plesset theory (MP2)[42] and the aug-cc-pVTZ basis set (denoted by AVTZ in this paper);[43] (b) a variational procedure of reduced dimensionality designed for the study of the far infrared (FIR) spectra of non-rigid molecules.[44–46] In this case, the starting point is a three-dimensional potential energy surface computed with CCSD(T)-F12b/CVTZ-F12.

2.2. The structure of peroxyacetic acid

The PAA molecule is a non-rigid molecule where three internal rotations, the methyl group torsion (θ), the torsion of the C–O single bond (α), and the hydroxyl group torsion (β) interconvert the equilibrium geometries. Fig. 1 can help to understand the torsional coordinates and the labelling of the atoms. The three torsional coordinates can be defined as a linear combination of curvilinear internal coordinates:

$$\begin{aligned}\theta &= (\mathrm{H7C2C1O3} + \mathrm{H8C2C1O3} + \mathrm{H9C2C1O3} - 2\pi)\\ \alpha &= \mathrm{O5O3C1C2}\\ \beta &= \mathrm{H6O5O3C1}\end{aligned} \quad (1)$$

A detailed search for equilibrium structures performed with CCSD(T)-F12b revealed three conformers, *Cc*, *Ct*, and *Ttg* for PAA. The capital letters *C* and *T* refer to the *cis* and *trans* relative positions of O4 and O5 atoms, whereas *c* and *t* refer to the *cis* and *trans* relative positions of the H6 and C1 atoms. *Cc* and *Ct* present a symmetry plane and can be classified in the C_s point group. Since the *Trans–trans–gauche* conformer (*Ttg* and *Ttg*′) corresponds to a double minimum, and the CH_3 torsion interconverts three equivalent minima, the ground state potential energy surface contains a total of 12 minima.

Table 1 summarizes the distinctive properties of the three PAA conformers: the CCSD(T)-F12b/AVTZ-F12 structural parameters and relative energies *E*, the equilibrium rotational constants, and the MP2/AVTZ components of the dipole moment with respect to the primary axis system which are compared with the experimental values of Cugley *et al.*[24] The *E* energies were vibrationally corrected to obtain E^{ZPVE} (see Fig. 2) considering the anharmonic zero-point vibrational energies (ZPVE), which were computed with MP2/AVTZ. Energies and structural parameters are provided in the ESI† (see Table S1).

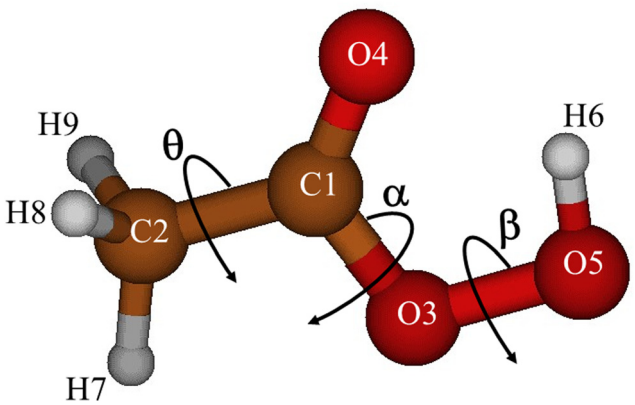

Fig. 1 The most stable *Cc* conformer of peroxyacetic acid.

The *Cc* conformer ($\theta = 0^\circ$, $\alpha = 180^\circ$, $\beta = 0^\circ$) exhibits notable stability due to the presence of an intramolecular hydrogen bond of 1.8511 Å between the oxygen atom of C=O and the hydrogen atom of OH. As was previously observed,[25,26,32] weak hydrogen bonds perturb the structural and spectroscopic properties of organic molecules. The excitation of the torsional modes causes the weak bond breaking, leading to the conformers *Ct* ($\theta = 0^\circ$, $\alpha = 180^\circ$, $\beta = 180^\circ$) and *Ttg* ($\theta = -172.6^\circ$, $\alpha = -0.3^\circ$, $\beta = -138.7^\circ$), which lie 1627.7 cm^{-1} and 2015.9 cm^{-1} above *Cc*, respectively. This explains why previous experimental studies focused on *Cc* neglecting the secondary minima. Additionally, the *Ttg* conformer is less stable than *Ct* due to non-bonding repulsions between the hydrogen atoms of OH and methyl group.

Torsional barriers are shown in Table 1. Fig. 3 shows the energy variation with the methyl torsional coordinate θ. The curves were computed by fixing α and β to their respective values in the three conformers, for which the V_3 barriers are estimated to be 88.6 cm^{-1} (*Cc*), 33.4 cm^{-1} (*Ct*), and 624.2 cm^{-1} (*Ttg*). For the most stable conformer *Cc*, our computed parameters are in good agreement with the experimental data of Cugley *et al.*[24] (V_3 = 76.70(45) cm^{-1}) derived from the assignment of the microwave spectrum. This value is half of what was calculated for the most stable conformer of acetic acid (V_3 = 169.8 cm^{-1}),[46] which is also quite low. A quite complicated distribution of the low methyl torsional energy levels and their splittings can be expected.

As was first computed for methyl isocyanate (V_3 = 16.2 cm^{-1})[47] and *trans*-methyl formate (V_3 = 26 cm^{-1}),[48] the V_3 barrier of the *Ct* conformer is so low that the methyl group torsion can be understood as a free internal rotation. In the *Ttg* conformer, the interaction between the methyl and OH groups increase the parameters to a magnitude similar to that of several sulfur analogs of methyl hydroperoxide, showing V_3 barriers of 685.52 cm^{-1} (CH_3–O–S–H), 696.6 cm^{-1} (CH_3–S–O–H), and 584.3 cm^{-1} (CH_3S–S–H).[49]

The two profiles in Fig. 4 represent the variation in energy with respect to the α coordinate (C–O bond torsion). These were computed by fixing the θ and β angles at $\theta = 0^\circ$ and $\beta = 0^\circ$ or 180°. The profile corresponding to $\beta = 180^\circ$ represents a minimum energy pathway for the *Ct* → *Ttg* interconversion, which is restricted by a barrier of V^{CO} ($\beta = 180^\circ$) estimated to be 4875 cm^{-1}. The barrier V^{CO} ($\beta = 0^\circ$) has been estimated to be 8707 cm^{-1}.

The profiles in Fig. 5 represent the energy variation with the β coordinate (OH torsion), while the remaining coordinates were frozen; in A, $\theta = 0^\circ$ and $\alpha = 180^\circ$ correspond to the values of these angles in the *Cc* and *Ct* conformers, and in B, $\theta = 180^\circ$ and $\alpha = 0^\circ$ correspond to the *Ttg* region of the ground electronic state potential energy surface. While the interconversion of *Cc* → *Ct* is restricted by a relatively high value (~1896 cm^{-1}), the reverse process *Ct* → *Cc* shows a quite low value (~150 cm^{-1}) that justifies why *Ct* is not observed. Some of these values allow the comparison with acetic acid, where the *cis* geometry is

Table 1 The CCSD(T)-F12b/CVTZ-F12 relative energies (E, E^{ZPVE}, in cm^{-1}), internal rotation barriers (in cm^{-1}), and the equilibrium structural parameters of PAA. MP2/AVTZ dipole moments (in D)

	Cc	*Ct*	*Ttg*		*Cc*		*Ct*	*Ttg*
	Calc.	Calc.	Calc.		Calc.	Exp 24	Calc.	Calc.
E	*0.0*	1869.0	2194.1	μ_a	2.4767	2.294(3)	0.4316	2.9103
E^{ZPVE}	0.0	1627.7	2015.9	μ_b	0.7865	0.650(4)	3.5705	2.3005
θ	0.0	0.0	−172.6	μ_c	0.0	0.0	0.0	−1.0907
α	180.0	180.0	−0.3	μ_t	2.5986	2.384(5)	3.5965	3.8668
β	0.0	180.0	−138.7					
A_e	10 922.45	10 676.60	9326.98	V_3	88.6	76.70(45)	33.4	624.2
B_e	4317.58	4211.56	4565.86	V^{CO} ($\theta = 0°$, $\beta = 0°$)				8707
C_e	3154.83	3077.72	3138.29	V^{CO} ($\theta = 0°$, $\beta = 180°$)				4875
				V^{barr} ($C_c \rightarrow C_t$)				1896
				$V^{OH}\left(T_{tg} \rightarrow T'_{tg}\right)$				26

	Cc	*Ct*	*Ttg*		*Cc*	*Ct*	*Ttg*
Equilibrium structural parameters (distances, in Å, angles, in degrees)							
C2C1	1.4940	1.5023	1.4955	H7C2C1	111.4	108.2	107.6
O3C1	1.3465	1.3632	1.3734	H8C2C1	108.4	108.2	110.4
O4C1	1.2061	1.1921	1.1952	H9C2C1	108.4	112.1	110.3
O5O3	1.4347	1.4460	1.4506	O4C1C2O3	180.0	180.0	179.2
H6O5	0.9806	0.9645	0.9639	O5O3C1C2	180.0	180.0	−0.30
H7C2	1.0850	1.0871	1.0840	H6O5O3C1	−0.0	180.0	221.3
H8C2	1.0872	1.0871	1.0872	H7C2C1O3	−0.0	121.4	182.4
H9C2	1.0872	1.0852	1.0871	H8C2C1H7	121.3	121.3	120.9
O3C1C2	111.1	108.6	117.7	H9C2C1H7	−121.3	−121.3	−120.6
O4C1C2	127.0	126.9	126.5				
O5O3C1	110.4	108.7	111.0	H6–O4	1.8511		
H6O5O3	100.0	97.6	98.6				

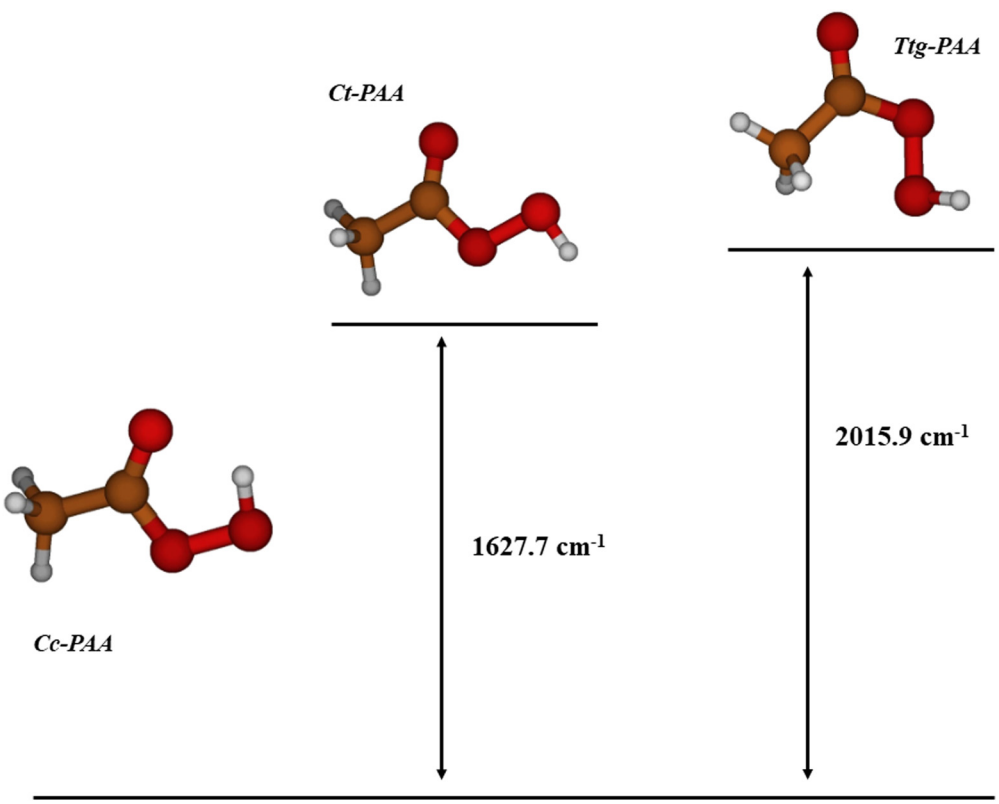

Fig. 2 Relative stability of the three PAA conformers.

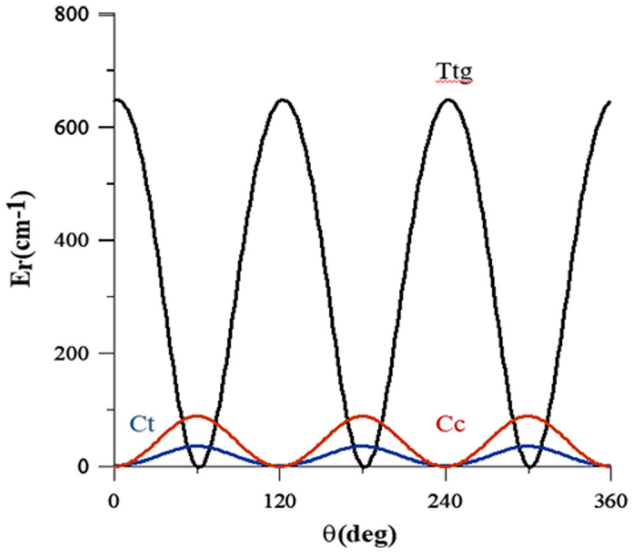

Fig. 3 V_3 methyl torsional barriers computed using CCSD(T)-F12b/CVTZ-F12. Energies are given relative to the *Cc* global minimum.

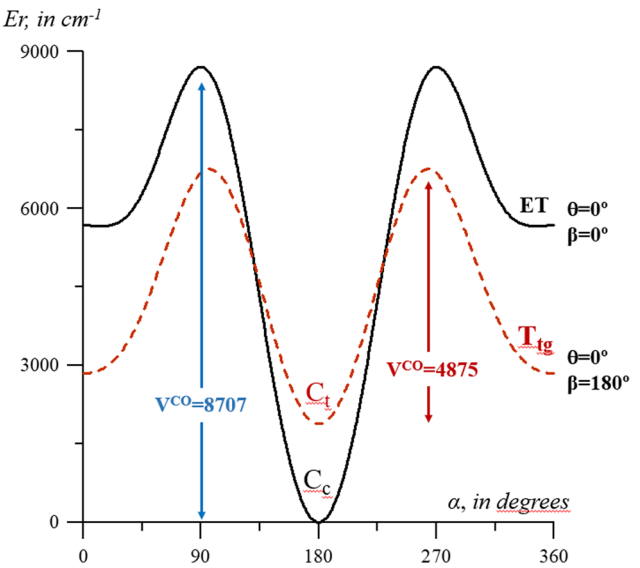

Fig. 4 One-dimensional potential energy surfaces $V(\alpha, \beta = 0^\circ, \theta = 0^\circ)$ and $V(\alpha, \beta = 180^\circ, \theta = 0^\circ)$. Energies are given relative to the *Cc* global minimum.

1883 cm^{-1} over the favor *trans*-conformation and the $T \rightarrow C$ process is restricted by a barrier of 4432 cm^{-1}.[46]

As evident, the two profiles of Fig. 5, A and B, are extremely different. In B, β varies from 120° to 240° to emphasize the very low barrier of the *Ttg* → *Ttg′* process, although $V(\beta)$ reaches 4739 cm^{-1} at $\beta = 0^\circ$. This occurs because the C–O and OH torsional modes are strongly coupled. This study reveals that the three torsions interact and are not separable. Additionally, the methyl group torsion and the C–O torsion are not negligible. Fig. 6 represents a two-dimensional potential energy surface that depends on α and β. The anisotropy of this figure highlights the relevance of the torsional coupling between these two torsional motions.

2.3. VPT2 vibrational analysis

For the 21 vibrational modes, the fundamental frequencies were obtained from the vibrational energies computed using the equation:

$$E = \sum_i \omega_i \left(v_i + \frac{1}{2}\right) + \sum_{i \geq j} x_{ij} \left(v_i + \frac{1}{2}\right)\left(v_j + \frac{1}{2}\right) \quad (2)$$

where ω_i represents the harmonic fundamentals computed and x_{ij} represents the anharmonic constants computed using VPT2 and the MP2/AVTZ anharmonic force field.[40] ν_i and ν_j represent the vibrational quanta. For the most stable conformer, the harmonic fundamentals have been computed using both MP2/AVTZ and CCSD(T)-F12/CVTZ-F12. The final anharmonic parameters are denoted by Calc (MP2) and Calc′ (CCSD(T)-F12 + MP2).

In Table 2, they are summarized and compared with experimental data in the case of *Cc* for which these data are available. Unfortunately, the experimental data of Table 2 were measured in Ar matrices.[23] It must be pointed out that the VPT2 theory predicts significant shifts due to Fermi resonances in the transitions emphasized in bold. To perform the test of Fermi resonances, we have built and diagonalized a large matrix composed of all singly excited states, doubly excited states (within a single vibrational mode) and 1 + 1 combinations, together with all off-diagonal Fermi coupling matrix elements by diagonalizing a matrix which has been built with the energy levels corresponding to excitations of one or two vibrational modes (diagonal terms) and the cubic force field (out-diagonal terms).

The presence of an intermolecular hydrogen bond in the *Cc* conformer is indicated by the OH stretching fundamental, which band center was computed at 3285 cm^{-1} (MP2) and 3317 cm^{-1} (CCSD(T)-F12 + MP2) and observed at 3282 cm^{-1},[23] below the corresponding bands of *Ct* (3597 cm^{-1}) and the one for *Ttg* (3596 cm^{-1}).

The band center of $2\nu_{OH}$ and $3\nu_{OH}$ bands of *Cc* peroxyacetic acid have been measured using a combination of FT-IR and photoacoustic spectroscopy[26] at 6315 cm^{-1} and 9037 cm^{-1}, respectively[26] whereas our computations place them at $2\nu_{OH}$ = 6346 cm^{-1} and $3\nu_{OH}$ = 9185 cm^{-1} (MP2). Furthermore, VPT2 place the $2\nu_{OH}$ overtone at 8031 cm^{-1} and 7030 cm^{-1}, in *Ct* and *Ttg*, respectively.

The weak intramolecular bond has an important effect on the OH-torsional fundamental, ν_{19}, computed to be 428 cm^{-1} (MP2) and to be 419 cm^{-1} (CCSD(T9-F12 + MP2) in *Cc* and to be ~92 and 26 cm^{-1} in *Ct* and *Ttg*, respectively. The mode ν_{19} was observed by Cugley *et al.*[23] at 422 cm^{-1} in the Ar matrix.

Unfortunately, the comparison between computation and the available experimental data for the torsional modes[23] is difficult, mainly because the corresponding band observed in Ar matrices is expected to be displaced to higher frequencies with respect to the measurements in the gas phase which are unavailable. For this reason, to obtain reliable results, we opted for a variational procedure instead of the VPT2 theory, which is developed specifically for semi-rigid species.

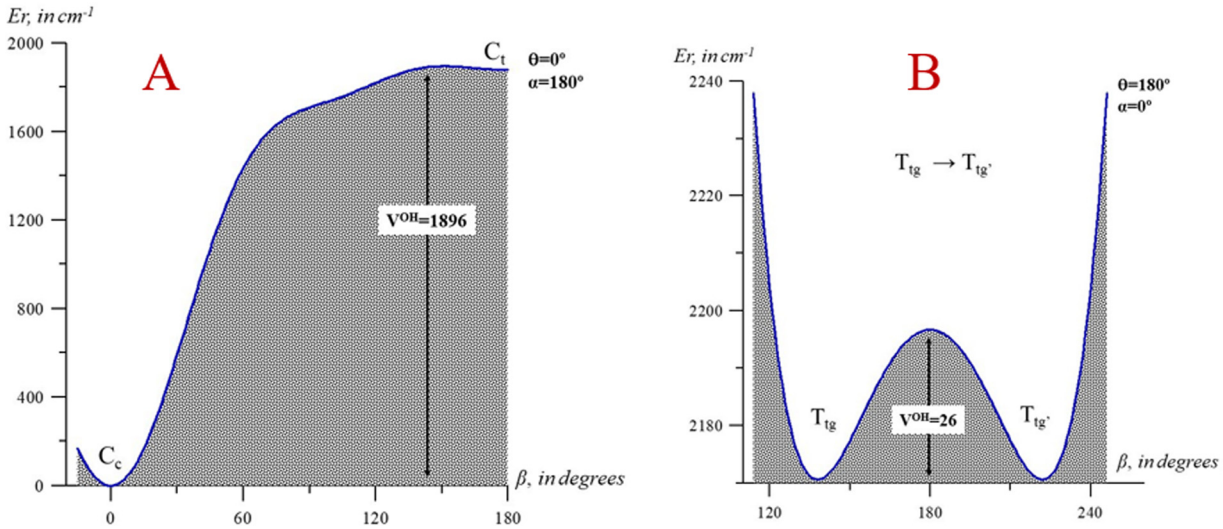

Fig. 5 One-dimensional cuts of the 3D-PES depending on the β coordinate (OH torsion). (A) $V(\beta, \theta = 0°, \alpha = 180°)$; (B) $V(\beta, \theta = 180°, \alpha = 0°)$. Energies are given relative to the *Cc* global minimum.

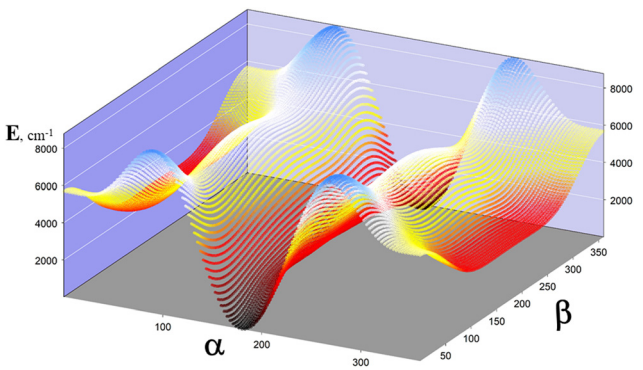

Fig. 6 Two-dimensional potential energy surface of peroxyacetic acid depending on α and β.

Table 2 displays the harmonic fundamental ω_{19} = 92 cm^{-1} instead of ν_{19} for which the MP2/AVTZ value is unrealistic due to the shape of the potential energy surface in the region of *Ct* that favours the *Ct* → *Cc* interconversion (see the A-profile of Fig. 5) and introduces errors in the computations of fourth-order numerical derivatives and the anharmonic force field.

2.4. Ground vibrational state: rotational and centrifugal distortion constants

The vibrational ground state rotational constants reported in Table 3 were calculated from the CCSD(T)-F12b equilibrium rotational constants using the following equation:

$$B_0 = B_e(\text{CCSD(T)-F12b/CVTZ-F12}) + \Delta B^{\text{vib}}(\text{MP2})/\text{AVTZ} \qquad (3)$$

previously tested for another molecules.[34,35] Here, ΔB^{vib} represents the vibrational contribution derived from the MP2/AVTZ cubic force field. The vibrational second-order perturbation theory was used to calculate the α_r^i vibration–rotation interaction parameters.

Table 2 MP2/AVTZ anharmonic fundamental frequencies (in cm^{-1})[a] calculated in this work (Calc.) and measured in previous experiments in the gas phase of PAA. The set of frequencies Calc′ has been determined using the CCSD(T)-F12 harmonic fundamentals and the MP2/AVTZ force field

		Cc (C_s)			*Ct* (C_s)	*Ttg*(C1)	
Mode	Assign.[b]	Calc.	Calc.′	Exp.[c]	Calc.		Calc.
A′						A	
1	OH-st	**3284**	3317	3282	3597		3596
2	CH_3-st	3074	3033	3025	3070		3079
				3005			
				2995			
3	CH_3-st	2992	2962		**2981**		2991
4	C═O-st	**1763**	**1769**	1767	1809		1797
5	CH_3-b	1459	**1460**	1439	1456		1445
6	HOO-b	1443	1447		1364		1374
7	CH_3-b	1371	1371	1369	1363		1351
8	C–O-st	1235	1242	1234.3	1184		1204
9	HCC-b	1011	1009	940	996		994
10	C–O-st	965	955	865	928		927
11	HCC-b	868	874		827		785
12	C–C-st	647	644	618.8	**625**		556
13	OCO-b	430	432	449	415		487
14	OOC-b	318	319	318.5	296		**325**
A″							
15	CH_3-st	3057	**3018**		**3055**	A	3048
16	CH_3-b	1448	1438		**1452**		1436
17	CH_3-b	1040	1037	1040	1038		1042
18	CH_3-b	617	615	646.5	589		546
19	OH-tor	428	419	422	92[d]		26
20	C–O tor	220	213		195		154
21	CH_3-tor	52	61		63		175

[a] Emphasized in black, the frequencies for which displacements by Fermi resonances can be relevant. [b] st = stretching; b = bending; w = wagging; tor = torsion. [c] Measured in the Ar matrix;[23] the experimental frequencies are those selected by the authors used in the force constant calculation. [d] Harmonic fundamentals, ω.

To our knowledge, experimental rotational constants are only available for the preferred conformer (*Cc*) whose stability is prominent. For this structure, the agreement between the

Table 3 Ground vibrational state rotational constants (computed with eqn (3)) and centrifugal distortion constants corresponding to the asymmetrically reduced Hamiltonian parameters in the III_r representation

	Cc		*Ct*	*Ttg*
	Calc.	Exp[23]	Calc.	Calc.
In MHZ				
A_0	10 821.92	10 814.95	10 535.79	9263.06
B_0	4276.17	4275.06	4173.37	4529.61
C_0	3125.52	3122.64	3051.14	3106.31
In KHz				
Δ_J	760.959		800.013	870.364
Δ_K	673.708		170.200	200.167
Δ_{JK}	391.100		892.416	463.298
δ_J	206.666		214.054	255.165
δ_K	−947.367		656.527	304.396
In Hz				
ϕ_J	0.4883		0.6246	−0.1239
ϕ_K	−0.1353		−0.1830	0.2724
ϕ_{JK}	−0.8139		−0.7126	0.2170
ϕ_{KJ}	0.1174		0.9239	−0.1364
ϕ_J	0.4892		0.5053	0.2051
ϕ_K	−0.4072		−0.3733	0.2865
ϕ_{JK}	−0.5334		−0.8744	0.2046

theoretical and experimental rotational constants is excellent. The computed parameters A_0 = 10 821.92 MHz, B_0 = 4276.17 MHz and C_0 = 3125.52 MHz compare well with those of Cugley *et al.*,[24] A_0 = 10 814.95 MHz, B_0 = 4275.06 MHz, C_0 = 3122.64 MHz), derived from microwave spectroscopy. Dissimilarities $\Delta B_0 = |B_{Exp} - B_{Calc}|$ are very small ($\Delta A_0 \sim 7$ MHz, $\Delta B_0 \sim 1$ MHz and $\Delta C_0 \sim 3$ MHz). Divergences coincide with previous studies of other molecules such as methyl glyoxal or methyl vinyl ketone, performed at the same level of theory.[34]

The MP2/AVTZ force field was used to compute the quartic and sextic centrifugal distortion constants shown in Table 3. They are parameters of the Watson asymmetrically reduced Hamiltonian (III_r representation).[50]

2.5. The Far Infrared region

Searching for an accurate description of the Far Infrared region, the low-lying vibrational energy levels that correspond to the three internal rotations were computed by solving a three-dimensional Hamiltonian which obeys the formula:[44–46]

$$H(\theta,\alpha,\beta) = -\sum_{i=1}^{3}\sum_{j=1}^{3}\left(\frac{\partial}{\partial q_i}\right)B_{q_iq_j}(\theta,\alpha,\beta)\left(\frac{\partial}{\partial q_j}\right) + V^{\text{eff}}(\theta,\alpha,\beta) \quad (4)$$

Here, q_i, q_j = θ, α, β. This Hamiltonian was defined by considering the predictions of the test of resonances described in previous sections which confirm the separability of the torsional modes with respect to the remaining vibrations. In eqn (4), $B_{q_iq_j}$ and V^{eff} represent the kinetic energy parameters[44] and the vibrationally corrected effective potential defined as the sum of three contributions:

$$V^{\text{eff}}(\theta,\alpha,\beta) = V(\theta,\alpha,\beta) + V'(\theta,\alpha,\beta) + V^{\text{ZPVE}}(\theta,\alpha,\beta) \quad (5)$$

Here, $V(\theta,\alpha,\beta)$ represents the *ab initio* three-dimensional potential energy surface, and $V'(\theta,\alpha,\beta)$ and $V^{\text{ZPVE}}(\theta,\alpha,\beta)$ represent the Podolsky pseudopotential and the zero-point vibrational energy correction, respectively.

The *ab initio* three-dimensional potential energy surface, $V(\theta,\alpha,\beta)$, was constructed using the total electronic energies of 156 geometries selected for different values of H7C2C1O3 (0°, 180°, and ±90°), O5O3C1C2 (0°, 30°, 60°, 90°, 120°, 150°, 180°) and H6O5O3C1 (0°, ±30°, ±60°, ±90°, ±120°, ±150°, 180°) dihedral angles. In all the geometries, $3N_a$-9 internal coordinates (N_a = number of atoms) were allowed to be relaxed at the MP2/AVTZ level of theory. The 156 structures are provided in the ESI† (see Table S4). Energies were computed in CCSD(T)-F12b/CVTZ-F12 single point computations on the 156 geometries. The zero-point vibrational correction $V^{\text{ZPVE}}(\theta,\alpha,\beta)$ was computed at the MP2/AVTZ level of theory within the harmonic approximation.[51] This approximation has been tested in previous papers for which experimental data measured in the gas phase are available. Generally, its consideration improves the computed frequencies. In the case of PAA, if the vibrational correction is considered, the fundamental levels displace ∼0.5 cm^{-1} (methyl torsion), ∼1 cm^{-1} (C–O bond torsion) and ∼−6 cm^{-1} (OH torsion). $V'(\theta, \alpha, \beta)$ adds a negligible correction of the 3D-PES.

A triple Fourier series transforming as the totally symmetric representation of the G_{12} Molecular Symmetry Group (MSG)[33] was selected to represent analytically the effective potential:

$$V^{\text{eff}}(\theta,\alpha,\beta) = \sum_{K,L,M} A^{\text{CCC}}_{KML}\cos M\theta\cos L\alpha\cos K\beta A^{\text{SSS}}_{KML}\sin M\theta\sin L\alpha\sin K\beta + A^{\text{CSS}}_{KML}\cos M\theta\sin L\alpha\sin K\beta + A^{\text{SCS}}_{KML}\sin M\theta\cos L\alpha\sin K\beta + A^{\text{SSC}}_{KML}\sin M\theta\sin L\alpha\cos K\beta \quad (6)$$

The 156 vibrationally corrected energies were fitted to obtain the 132 coefficients which are provided in the ESI† (see Table S2). The parameters of the linear fit reached $\sigma = 0.82 \times 10^{-4}$ and R^2 = 0.9999; the coefficients of $\cos 3\theta\cos 3\alpha$ (121.356 cm^{-1}) and $\sin 3\theta\sin 3\alpha$ (−138.752 cm^{-1}) denote important resonances between the methyl and the C–O bond torsions although those describing the interaction between the methyl and the OH torsion (terms type $\cos 3\theta\cos K\beta$) are quite small. Contributing coefficients describing the interactions between the CC-bond and the OH torsions are obtained (*i.e.* 976.139 $\cos 3\alpha\cos 3\beta$).

Analytical expressions containing 132 terms and formally identical to eqn (6) were employed for the fitting of the kinetic energy parameters, $B_{q_iq_j}$. The expansion coefficients are provided in the ESI† (see Table S3). The most contributed ones are the A^{CCC}_{000} coefficients determined to be $A_{000}(B_{\theta\theta})$ = 5.6243 cm^{-1}, $A_{000}(B_{\alpha\alpha})$ = 1.5428 cm^{-1}, $A_{000}(B_{\beta\beta})$ = 20.0919 cm^{-1}, $A_{000}(B_{\theta\alpha})$ = −0.1618 cm^{-1}, $A_{000}(B_{\theta\beta})$ = 0.0009 cm^{-1}, and $A_{000}(B_{\alpha\beta})$ = −0.7741 cm^{-1}.

The Hamiltonian of eqn (4) was solved variationally using symmetry adapted Fourier series. Since the stability of the *Cc* conformer is prominent, all the low energies below 600 cm^{-1} can be assigned to this minimum. The energies of Table 4 are

Table 4 Low-lying vibrational energy levels of the *Cc* conformer of PAA up to 600 cm^{-1}. In italic, VPT2 energies computed from the CCSD(T)-F12 anharmonic fundamentals and the MP2 anharmonic force field

	Variational					Variational			
ν_{21} ν_{20} ν_{19}	3D		1D	VPT2	ν_{21} ν_{20} ν_{9}	3D		1D	VPT2
0 0 0	A_1	0	0	0	ν_{13} (A′)				
	E	2.262	2.102						
1 0 0	A_2	49.082	55.421	51.8	0 2 0	A_1	429.798	354.402	437.5
	E	35.676	39.544	*60.5*		E	437.135		*422.8*
2 0 0	A_1	73.105	73.166	104.5	1 0 1	A_1	440.798		474.3
	E	99.917	103.556	*121.9*		E	426.397		*474.2*
3 0 0	A_2	202.581	214.643	158.1	4 0 0	A_2	462.825	468.992	—
	A_1	201.735	215.111	212.6		A_1	473.365	468.414	
	E	146.831	153.32	*184.2*		E	532.722	372.529	
	E	265.487	288	*247.4*		E	594.882	575.625	
0 1 0	A_2	216.673	177.883	220	2 0 1	A_2	463.636		
	E	220.721		*212.6*		E	490.757		
1 1 0	A_1	268.17		259.3	$3\nu_{21}$ ν_{14} (A″)				470.7
	E	324.459		*260.6*					*498.6*
2 1 0	A_2	288.912		299.5	ν_{21} ν_{13} (A″)				482.5
	E	329.151		*309.5*					*493.5*
ν_{14} (A′)				317.5	1 2 0	A_2	499.658		464.3
				319.3		E	463.172		*458.3*
3 1 0	A_2	387.325		340.6	2 2 0	A_1	510.99		492
	A_1	388.021		*359.3*		E	517.926		*494.7*
	E	393.656			3 2 0	A_1	580.606		
	E	450.894				A_2	581.063		
ν_{21} ν_{14} (A″)				367.7		E	598.993		
				378.2					
$2\nu_{21}$ ν_{14} (A′)				418.7		E	>600		
				437.9					
0 0 1	A_2	393.635	372.367	428.1	3 0 1	A_2	591.438		569.3
	E	396.325				A_1	592.926		
						E	537.52		
						E	607.952		
					3D-ZPVE			335.392	

classified using three quanta $\nu_{21}\nu_{20}\nu_{19}$ and the representations of the G_6 subgroup of G_{12}. Due to tunnelling effects in the methyl torsion barriers, the energy levels split into three components, one non-degenerated A_i (i = 1, 2) and one twofold degenerate E. The energies are compared with results obtained using VPT2 and with one-dimensional calculations performed by solving one-dimensional Hamiltonians depending on θ, α or β,

$$H(\lambda) = -\left(\frac{\partial}{\partial\lambda}\right)B(\lambda)\left(\frac{\partial}{\partial\lambda}\right) + V^{\text{eff}}(\lambda) \quad \lambda = \theta, \alpha, \beta \qquad (7)$$

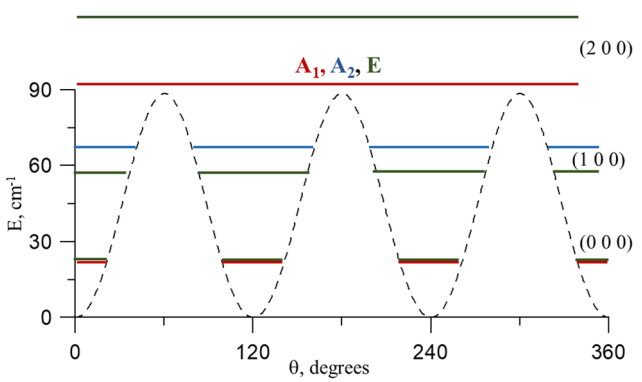

Fig. 7 Distribution of the methyl torsional energies in the 1-D potential energy surface.

whose kinetic parameters $B(\lambda)$ and $V^{\text{eff}}(\lambda)$ are provided as ESI† (see Tables S3a, b and S3). The distributions of the 3D-energy levels corresponding to vibrational excitations of the methyl torsional mode, are anarchic, specially for the E energies. We have employed the 1D levels to help with assignments. The ground vibrational state (0 0 0) splits into 3 components due to the presence of the methyl torsional barrier of V_3 = 88.6 cm^{-1}. The gap between non-degenerate and two-fold degenerate levels was obtained to be 2.262 cm^{-1}. The first excited energy (1 0 0) was found at 49.082 cm^{-1} (A_1) and 35.676 cm^{-1} (E). This places the fundamental transition at 49.1 cm^{-1} (A_1) and 33.4 cm^{-1} (E). The A component is in good agreement with the value computed with the full-dimensional VPT2 theory (51.8 cm^{-1} (MP2) and 60.5 cm^{-1} (CCSD(T)-F12 + MP2)). Fig. 7 can help to understand the level distributions. Energy levels (0 0 0) and (1 0 0) are below the barrier. From the overtone (2 0 0), the distribution of the non-degenerate energies behaves as a free rotor.

The first excited energy (0 1 0) for the ν_{20} mode (C–O bond torsion) has been found to be 216.673 cm^{-1} (A_2) and 220.721 cm^{-1} (E). These values are in good agreement with the VPT2 energy (220.0/212.6 cm^{-1}) but over the 1D-energy computed variationally (177.883 cm^{-1}). These results confirm that ν_{20} interacts strongly with the other two torsional modes, but slightly with the remaining vibrations, which were considered in the VPT2 model and neglected in the 3D-model.

The first excited energy (0 0 1) corresponding to the ν_{19} mode (OH torsion) has been computed to be 393.635 cm^{-1} (A_2) and 396.325 cm^{-1} (E) below the experimental value by Cugley *et al.*[23] (422 cm^{-1}) measured in the Ar matrix. Unfortunately, available experimental data is not sufficient for a complete comparison, but in general, measurements with this technique produce different frequencies than the gas phase measurements specially for LAMs. The one-dimensional energy value (372.367 cm^{-1}) is much lower than the three-dimensional one, as it was obtained for the C–O torsional fundamental.

The two overtones $2\nu_{21}$ (2 0 0), $2\nu_{20}$ (0 2 0), and $2\nu_{19}$ (0 0 2) have been computed to be 73.105 cm^{-1} (A_1) and 99.917 cm^{-1} (E), and 429.798 cm^{-1} (A_2) and 437.135 cm^{-1} (E), respectively. $2\nu_{19}$ (0 0 2) lies over 600 cm^{-1}.

In a first approximation and for very low temperatures, it may be inferred that the methyl internal rotation is the unique mode that can be treated in one dimension as usually done in assignments of experimental microwave spectra, where the employed effective Hamiltonians depend on a single or (at much) two large amplitude motions.

3. Conclusions

This study aims to provide a theoretical description of the structural spectroscopic properties of PAA. This species, for which there is a lack of previous information, represents an OOM present in urban areas. Like other peroxides, it contributes to increasing the oxidation capacity of the troposphere. The results can help further experimental studies required by the atmosphere chemistry research.

A detailed search for equilibrium structures performed with CCSD(T)-F12b revealed three conformers, *Cc*, *Ct*, and *Ttg*. The *Cc* conformer exhibits notable stability due to the presence of an intramolecular hydrogen bond of 1.8511 Å between the oxygen atom of C═O and the hydrogen atom of OH. The excitation of the three torsional modes causes the breaking of the weak bond, leading to the conformers *Ct* and *Ttg* at 1627.7 cm^{-1} and 2015.9 cm^{-1} above *Cc*, respectively. The fact that both structures are neglected in previous experimental studies is sufficiently justified by the computed relative stabilities and the shape of the potential energy surface. The computed barriers restricting the conformer interconversion can help further kinetic studies.

The *Cc* ground vibrational state rotational constants have been computed to be A_0 = 10 821.92 MHz, B_0 = 4276. 17 MHz and C_0 = 3125. 52 MHz at a few MHz of the available experimental data. These parameters can help to understand the accuracy of the employed methodology.

This work provides molecular properties that can help to advance experimental spectroscopic research of PAA. We consider that the distribution of levels that we provide can rarely be obtained by experimental techniques, although their knowledge is necessary for a proper interpretation of measurements. We have obtained low-energy levels which transitions can be observed using many experimental techniques. We emphasize the part of the work describing the distribution of vibrational energies and their splittings in the potential energy surface because this distribution cannot be understood without the employment of theoretical techniques based on highly correlated *ab initio* methods.

In *Cc*, the methyl torsional barrier has been found to be very low, V_3 = 88.6 cm^{-1} producing a splitting of 2.262 cm^{-1} for the ground vibrational state. The distributions of the 3D-energy levels corresponding to low vibrational excitations of the methyl torsional mode, are anarchic, specially for the *E* energies. The fundamentals for the ν_{21} (methyl torsion), ν_{20} (C–O bond torsion) and ν_{19} (OH torsion) have been computed to be 49.1 cm^{-1} (A_i), 33.4 cm^{-1} (E), 216.7 cm^{-1} (A_2) and 218.5 cm^{-1} (E) and 393.6 cm^{-1} (A_2) and 394.1 cm^{-1}, respectively.

The VPT2 full-dimensional vibrational analysis predicts that Fermi resonances between low-lying torsional energy levels and other vibrations are very weak. This confirms the validity of the 3D variational model used for the study of the FIR spectrum and confirms that the addition of more independent coordinates is not necessary for computing low energies. It has to be considered that in the employed vibrational theory, the interactions between the 3 independent coordinates and the remaining $3N_a$-6-3 coordinates are partially considered when they are allowed to be relaxed in all the 156 selected geometries employed to construct the PES and when the ZPVE correction is added.

However, the variational study confirms that the ν_{20} torsional mode interacts strongly with the other two torsional modes ν_{19} and ν_{21}. In a first approximation and for very low temperatures, the methyl internal rotation is the unique mode that can be treated in one dimension as usually done in assignments of microwave spectra. In many cases, the effective Hamiltonians defined for the study of the rotational structure depend on a single or (at much) two large amplitude motions.

Conflicts of interest

There are no conflicts to declare.

Acknowledgements

This project has received funding from the European Union's Horizon 2020 research and innovation programme under the Marie Skłodowska-Curie grant agreement No 872081''. This research was supported by the Agencia Estatal de Investigación of Spain through the grant PID2020-112887GB-I00/AEI/10.13039/501100011033. The author acknowledges the CTI (CSIC) and CESGA and the ''Red Española de Computación'' for the grant RES-AECT-2022-3-0006 for computing facilities. S. B. and D. M. acknowledge the ''Conseil National de la Recherche Scientifique de Tunis'' for the exchange grants in 2022 and 2023.

References

1 C. E. Reeves and S. A. Penkett, *Chem. Rev.*, 2003, **103**, 5199.

2 F. Bianchi, T. Kurtén, M. Riva, C. Mohr, M. P. Rissanen, P. Roldin, T. Berndt, J. D. Crounse, P. O. Wennberg and T. F. Mentel, *et al.*, *Chem. Rev.*, 2019, **119**, 3472.
3 J. G. Calvert, A. Lazrus, G. L. Kok, B. G. Heikes, J. G. Walega, J. Lind and C. A. Cantrell, *Nature*, 1985, **317**, 27.
4 M. Krapf, I. E. Haddad, E. A. Bruns, U. Molteni, K. R. Daellenbach, A. S. H. Prévot, U. B. Baltensperger and J. Dommen, *Chem*, 2016, **1**, 603.
5 J. D. Crounse, K. A. McKinney, A. J. Kwan and P. O. Wennberg, *Anal. Chem.*, 2006, **78**, 6726.
6 P. O. Wennberg, T. F. Hanisco, L. Jaegle, D. J. Jacob, E. J. Hintsa, E. J. Lanzendorf, J. G. Anderson, R.-S. Gao, E. R. Keim and S. G. Donnelly, *et al.*, *Science*, 1998, **279**, 49.
7 M. Qin, Z. Chen, H. Shen, H. Li, H. Wu and Y. Wang, *Atmos. Environ.*, 2018, **183**, 144.
8 S. J. Fuller, F. P. H. Wragg, J. Nutter and M. Kalberer, *Atmos. Environ.*, 2014, **92**, 97.
9 X. Qiao, C. Yan, X. Li, Y. Guo, Y. Rujing, D. Chenjuan, L. Chang, N. Wei, W. Mingyi and C. Runlong, *et al.*, *Environ. Sci. Technol.*, 2021, **55**, 13646.
10 Y. Wang, P. Clusius, C. Yan, K. Dällenbach, R. Yin, M. Wang, X. C. He, C. Biwu and L. Yiqun, *et al.*, *Environ. Sci. Technol.*, 2022, **56**, 770.
11 X. Cheng, Y. J. Li, Y. Zheng, K. Liao, T. Zhu, C. Ye, X. Qiu, K. T. Koenig, Y. Ge and Q. Chen, *EGUsphere*, 2023.
12 A. Mellouki, T. J. Wallington and J. Chen, *Chem. Rev.*, 2015, **115**, 3984.
13 B. Nozière, M. Kalberer, M. Claeys, J. Allan, B. D'Anna, S. Decesari, E. Finessi, M. Glasius, I. Grgic and J. F. Hamilton, *et al.*, *Chem. Rev.*, 2015, **115**, 3919.
14 H. Wu, Y. Wang, H. Li, L. Huang, D. Huang, H. Shen, Y. Xing and Z. Chen, *Atmos. Environ.*, 2017, **164**, 61.
15 X. Zhang, Z. M. Chen, S. Z. He, W. Hua, Y. Zhao and J. L. Li, *Atmos. Chem. Phys.*, 2010, **10**, 737.
16 J. A. Lind, A. L. Lazrus and G. L. Kok, *J. Geophys. Res.*, 1987, **92**, 4171.
17 B. K. Keller, M. D. Wojcik and T. R. Fletcher, *J. Photochem. Photobiol., A*, 2008, **195**, 10.
18 R. J. Yokelson, J. D. Crounse, P. F. DeCarlo, T. Karl, S. Urbanski, E. Atlas, T. Campos, Y. Shinozuka, V. Kapustin and A. D. Clarke, *et al.*, *Atmos. Chem. Phys.*, 2009, **9**, 5785.
19 F. A. F. Winiberg, T. J. Dillon, S. C. Orr, C. B. M. Groß, I. Bejan, C. A. Brumby, M. J. Evans, S. C. Smith, D. E. Heard and P. W. Seakins, *Atmos. Chem. Phys.*, 2016, **16**, 4023.
20 B. C. Faust, K. Powell, C. J. Rao and C. Anastasio, *Atmos. Environ.*, 1997, **31**, 497.
21 H. B. Singh, L. J. Salas and W. Viezee, *Nature*, 1986, **321**, 588.
22 P. A. Giguère and A. W. Olmos, *Can. J. Chem.*, 1952, **30**, 821.
23 J. Cugley, R. Meyer and H. S. H. Günthard, *Chem. Phys.*, 1976, **18**, 281.
24 J. A. Cugley, W. Bossert, A. Bauder and H. S. H. Günthard, *Chem. Phys.*, 1976, **16**, 229.
25 M. K. Hazra and A. Sinha, *J. Phys. Chem. A*, 2011, **115**, 5294.
26 M. K. Hazra, X. Kuang and A. Sinha, *J. Phys. Chem. A*, 2012, **116**, 5784.
27 R. Benassi and F. Taddei, *THEOCHEM*, 1994, **303**, 83.
28 S. L. Khursan and V. L. Antonovsky, *Russ. Chem. Bull.*, 2003, **52**, 1908.
29 C. H. Langley and E. A. Noe, *THEOCHEM*, 2004, **682**, 215.
30 C. E. Miller and J. S. Francisco, *J. Phys. Chem. A*, 2004, **108**, 2930.
31 C. E. Miller and J. S. Francisco, *J. Phys. Chem. A*, 2001, **105**, 750.
32 R. Boussesi, M. L. Senent and N. Jaïdane, *J. Chem. Phys.*, 2016, **144**, 164110.
33 R. Boussesi and M. L. Senent, *Phys. Chem. Chem. Phys.*, 2020, **22**, 23785.
34 I. Toumia, S. Dalbouha, M. M. Al-Mogren, O. Yazidia, N. Jaïdane, M. Carvajal and M. L. Senent, *J. Phys. Chem. A*, 2022, **126**, 7230.
35 M. Salah, K. Marachi, N. Komiha and M. L. Senent, Theoretical spectroscopic study of isopropyl alcohol (CH_3–CHOH–CH_3), *Astrophys. J.*, 2024, **963**, 143.
36 T. B. Adler, G. Knizia and H. J. Werner, *J. Chem. Phys.*, 2007, **127**, 221106.
37 G. Knizia, T. B. Adler and H. J. Werner, *J. Chem. Phys.*, 2009, **130**, 054104.
38 H.-J. Werner, P. J. Knowles, *et al.*, MOLPRO, version 2022, a package of *ab initio* programs, see **https://www.molpro.net**.
39 J. G. Hill, S. Mazumder and K. A. Peterson, *J. Chem. Phys.*, 2010, **132**, 054108.
40 V. Barone, *J. Chem. Phys.*, 2005, **122**, 014108.
41 M. J. Frisch, G. W. Trucks, H. B. Schlegel, G. E. Scuseria, M. A. Robb, J. R. Cheeseman, G. Scalmani, V. Barone, B. Mennucci, G. A. Petersson, *et al.*, *GAUSSIAN 16, Revision C.01*, 2016.
42 C. Møller and M. S. Plesset, *Phys. Rev.*, 1934, **46**, 618.
43 R. A. Kendall, T. H. Dunning, Jr and R. J. Harrison, *J. Chem. Phys.*, 1992, **96**, 6796.
44 M. L. Senent, *Chem. Phys. Lett.*, 1998, **296**, 299.
45 M. L. Senent, *J. Mol. Spectrosc.*, 1998, **191**, 265.
46 M. L. Senent, *Mol. Phys.*, 2001, **99**, 1311.
47 S. Dalbouha, M. L. Senent, N. Komiha and R. Domínguez-Gómez, *J. Chem. Phys.*, 2016, **145**, 124309.
48 M. L. Senent, M. Villa, F. J. Meléndez and R. Domínguez-Gómez, *Astrophys. J.*, 2005, **627**, 567.
49 S. Dalbouha, M. L. Senent and N. Komiha, *J. Chem. Phys.*, 2015, **142**, 074304.
50 J. K. G. Watson, *J. Chem. Phys.*, 1968, **48**, 4517.
51 A. G. Császár, V. Szalay and M. L. Senent, *J. Chem. Phys.*, 2004, **120**, 1203.